AIAA JOURNAL
Vol. 45, No. 7, July 2007

Aero-Optical Environment Around a Conformal-Window Turret

Stanislav Gordeyev*
University of Notre Dame, Notre Dame, Indiana 46556
Martiqua L. Post† and Thomas McLaughlin‡
U.S. Air Force Academy, USAFA, Colorado 80840
Juan Ceniceros§
The Boeing Company, Albuquerque, New Mexico 87109
and
Eric J. Jumper¶
University of Notre Dame, Notre Dame, Indiana 46556

DOI: 10.2514/1.26380

This paper presents the aero-optical environment around a generic conformal-window turret formed from a hemisphere on a short cylindrical base. A suite of optical instruments consisting of a Malley probe, a conventional two-dimensional Shack–Hartmann wave-front sensor, and a new high-bandwidth, lower-resolution Hartmann wave-front sensor were used to measure the aberrations on the wave front of a laser beam emanating from the turret at various angles in both the forward and aft direction in the turret's zenith plane. The measurements were made over a range of Mach numbers from 0.35 to 0.45. Complementary steady- and unsteady-pressure measurements over a slightly larger range of Mach numbers were also made, along with a surface-flow-visualization study of the complex flowfield over and around the turret. The use of the suite of sensors allowed for the recognition and separation of the aberrating optical environment into components associated with stationary disturbances and convecting disturbances at the frequency of the turret's separated wake and at order-of-magnitude-higher frequencies associated with structures that form in the separated shear layers, respectively. The optical data separated in this way are valuable because of the implications for adaptive optics.

I. Introduction

A TURRET provides a seemingly convenient way of propagating a laser beam from an airborne platform; however, the turret's nonoptimal aerodynamic shape creates high levels of unsteadiness in both the attached flow over the turret and in the flow that separates off the bluff turret in its aft quadrant. Optical aberrations that are due to both the flow's unsteadiness and the turbulent structures that form in the turbulent regions of the flow impose undesirable wave-front distortions on a laser beam emanating from the turret, which have degrading effects on the systems that make use of the beam; these effects are referred to as *aero-optical* effects [1,2]. An earlier paper reported on the aero-optical aberrating environment around a flat-window turret [3]; this paper reports on the environment around a similar turret, but with a conformal window. Both turrets were in fully subsonic flows, that is, nowhere on either turret did the flow become transonic. Both turrets were generic, in the sense that they consisted of a short cylindrical base with a hemispherical top, but the turrets differed in that the flat-window turret had a surface discontinuity at the turret-window juncture, whereas the conformal-window turret had no surface discontinuity and the window had the same radius as the hemisphere, smoothly blending into it. Among other differences, this means that the flat-window turret presents a different geometry to the flow at every projection angle, whereas the flow over the conformal-window turret sees exactly the same geometry for every projection angle; this geometry difference creates different aberrating environments for an emanating laser beam, which is most significantly different over certain projection angles, and these differences will be pointed out in this paper. In addition to pointing out the differences and similarities in the aero-optical environment around a conform-window turret, the study reported in this paper made use of a new time-resolved, high-bandwidth, two-dimensional, wave-front sensor that has greatly enhanced our understanding of the nature of the unsteady aberrating environment, both in the aft quadrant of the turret, on which the earlier paper concentrated, and in the forward quadrant of the turret, which has significant implications toward the use of the adaptive-optic systems [4] used to improve the beam's figure after emerging from the aberrating flow.

Even without the complications of a surface discontinuity, the flow around a conformal-window turret is complicated; Fig. 1 shows a schematic of some of the flow features that contribute to its aberrating nature. Starting upstream of the turret, the vorticity in the incoming boundary layer rolls up into a necklace vortex that stretches around the base of the turret and ends up interacting with the flow in the aft portion of the turret. This interaction allows for movement of the vortex in the forward section of the turret, effectively communicating the unsteadiness in the wake to the oncoming flow that then impinges on the forward quadrant of the turret and convects over the turret carrying the necklace-communicated unsteadiness with it; this and the oscillating stagnation point influenced by the unsteady separated wake off the lower portions of the turret in the aft quadrant impose unsteady aberrations on a beam projected from the forward quadrant of the turret at the frequencies of the wake's unsteadiness. As the attached flow first accelerates up to the outermost portion of

Presented as Paper 3074 at the 37th AIAA Plasmadynamics and Lasers Conference, San Francisco, CA, 5–8 June 2006; received 13 July 2006; revision received 25 February 2007; accepted for publication 7 March 2007. Copyright © 2007 by Gordeyev, Post, McLaughlin, Ceniceros, and Jumper. Published by the American Institute of Aeronautics and Astronautics, Inc., with permission. Copies of this paper may be made for personal or internal use, on condition that the copier pay the $10.00 per-copy fee to the Copyright Clearance Center, Inc., 222 Rosewood Drive, Danvers, MA 01923; include the code 0001-1452/07 $10.00 in correspondence with the CCC.

*Research Assistant Professor, Department of Aerospace and Mechanical Engineering. Member AIAA.
†Assistant Professor, Department of Aeronautics. Member AIAA.
‡Director of Research, Department of Aeronautics. Associate Fellow AIAA.
§Program Manager, Joint Technology Office, Aero-Optics. Young Professional Member AIAA.
¶Professor, Department of Aerospace and Mechanical Engineering. Fellow AIAA.

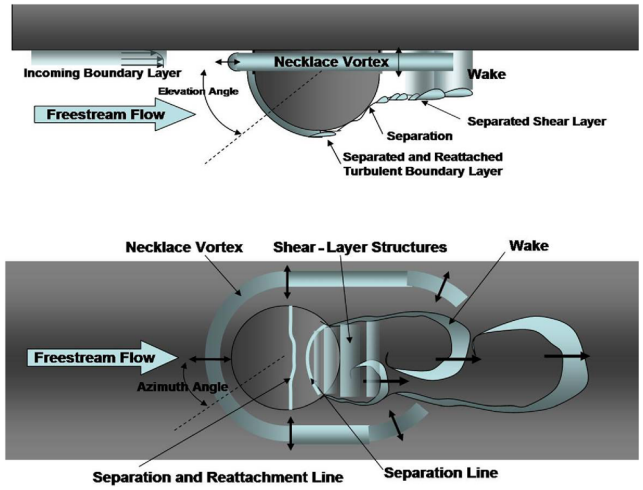

Fig. 1 Flow topology around the conformal-window turret.

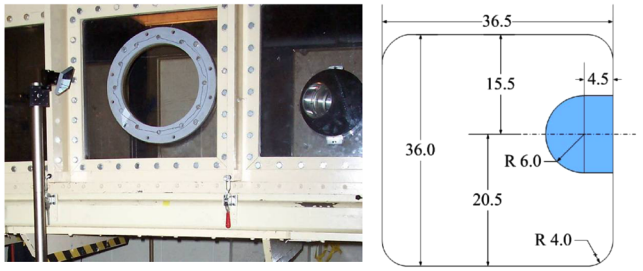

Fig. 2 Turret mounted on the back side of the tunnel (left); dimensional drawing of the tunnel's cross-section with the mounted turret (right, view looking upstream).

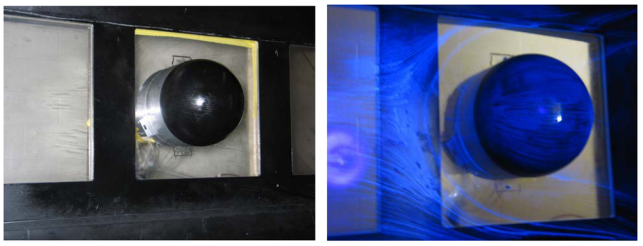

Fig. 3 Typical view of flow patterns under normal (left) and black (right) light.

the turret and then begins to decelerate, its pressure and density first drop and then begin to recover; because the index of refraction of air is directly related to the air's density through the Gladstone–Dale constant [1,2], this acceleration/deceleration causes an aerodynamic-lensing effect on the beam, which is unsteady due to the unsteadiness imposed by the necklace-related effects discussed earlier.

Once the deceleration begins and the attached boundary layer is exposed to the concomitant unfavorable pressure gradient, it eventually separates; this separation line is both unsteady and Reynolds-number-dependent. At low Reynolds numbers, the flow undergoes a laminar separation that occurs between 100 and 110 deg, but at a sufficiently high Reynolds number, the flow separates and reattaches as a turbulent boundary layer that does not again separate until about 120 deg (see [5], for instance). This turbulent separation is also unsteady, but its mean location was found to become essentially Reynolds-number-independent above a sufficiently high Reynolds number; the study presented here was above that Reynolds number. Once the flow has separated, its separated shear layers form Kelvin-Helmholtz-driven shear-layer structures shortly after separation, which eventually merge into the larger-scale wake structures. The shear layer and wake structures impose such a significant level of aberration on the laser beam that they effectively eliminate large portions of the aft quadrant from the turret's useful field of regard.

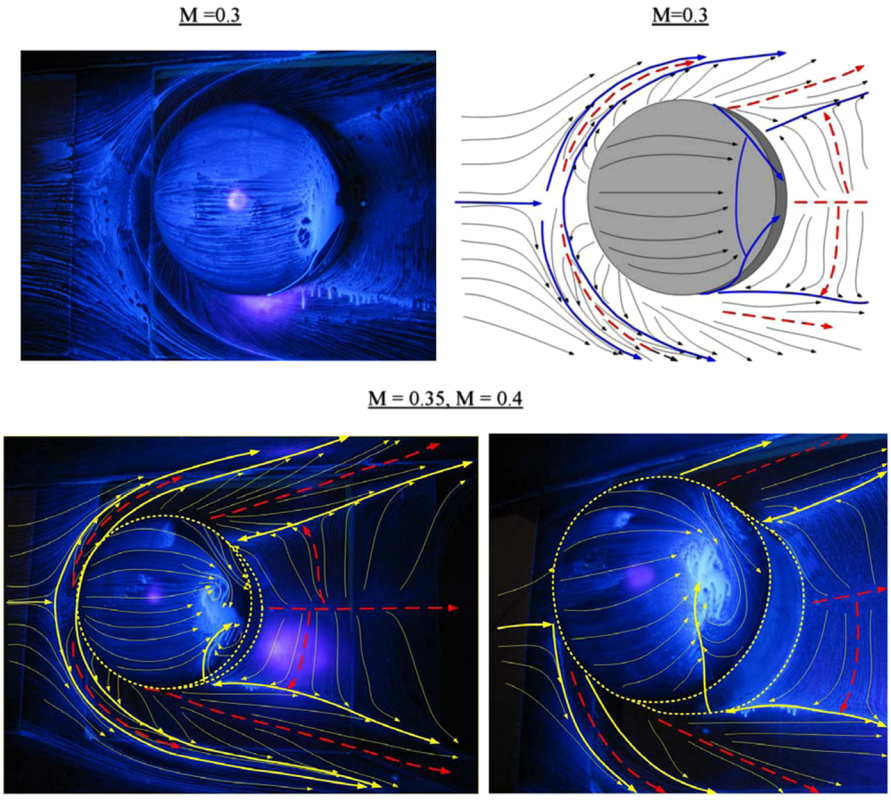

Fig. 4 Surface-flow topology on and around the turret: flow visualization (right) and schematic of surface streaklines (thin solid lines), stable (thick solid lines), and unstable (thick dashed lines) manifolds for different Mach numbers; turret contour is outlined by a dotted line.

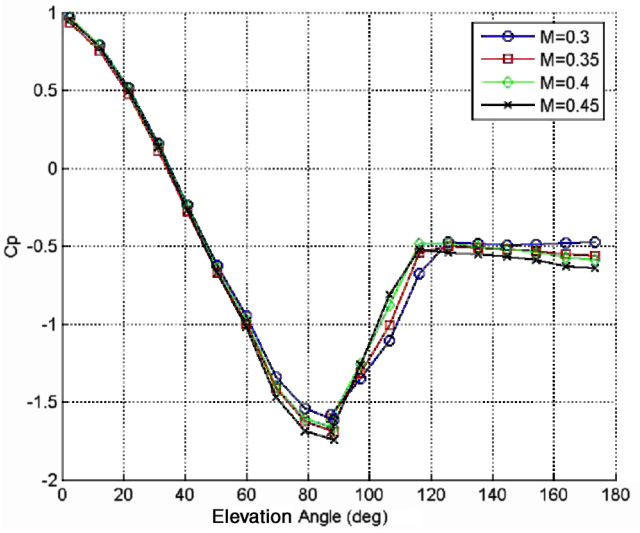

Fig. 5 Normalized static pressures along the line of the 0-deg azimuthal angle.

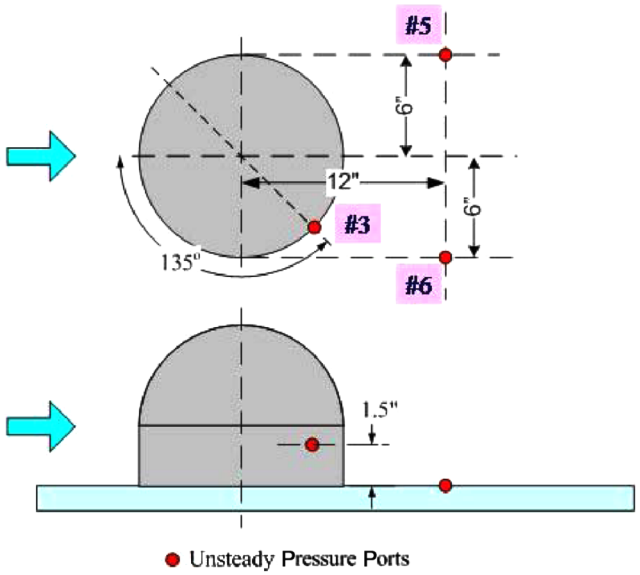

Fig. 6 Locations of unsteady-pressure sensors.

For the flat-window turret, the discontinuity at the turret-window junction forces the flow to separate from the turret at around 100 deg; because the separation is geometry-induced, unlike the conformal-window turret, it is Reynolds-number-independent [3]. In an earlier flat-window-turret study, passive flow control devices placed upstream of the turret-window junction were able to delay the separation to the angle at which the conformal-window turret separates without the aid of flow control [6].

This paper will describe the fluid mechanical and optical environments around a conformal-window turret as measured for the turret projecting into a subsonic wind tunnel. A description of the tunnel and turret will first be given, followed by a more complete description of the flow topology around the turret observed by flow visualization and by steady- and unsteady-pressure measurements. Following this, the optical experiment will be described and the results obtained using a suite of instruments including a Malley probe, an un-time-resolved two-dimensional wave-front sensor, and a new high-bandwidth, time-resolved, wave-front sensor developed jointly by Notre Dame University and Oceanit, followed by a comparison of the data from each sensor, from which some conclusions are made about the nature of the unsteady aero-optic environment around the turret.

II. Experimental Setup

The experiments were conducted in the subsonic wind tunnel at the U.S. Air Force Academy. This tunnel has a $3 \times 3 \times 8$ ft test section and is capable of achieving Mach numbers up to 0.5, although run times at Mach numbers above 0.45 are too short to

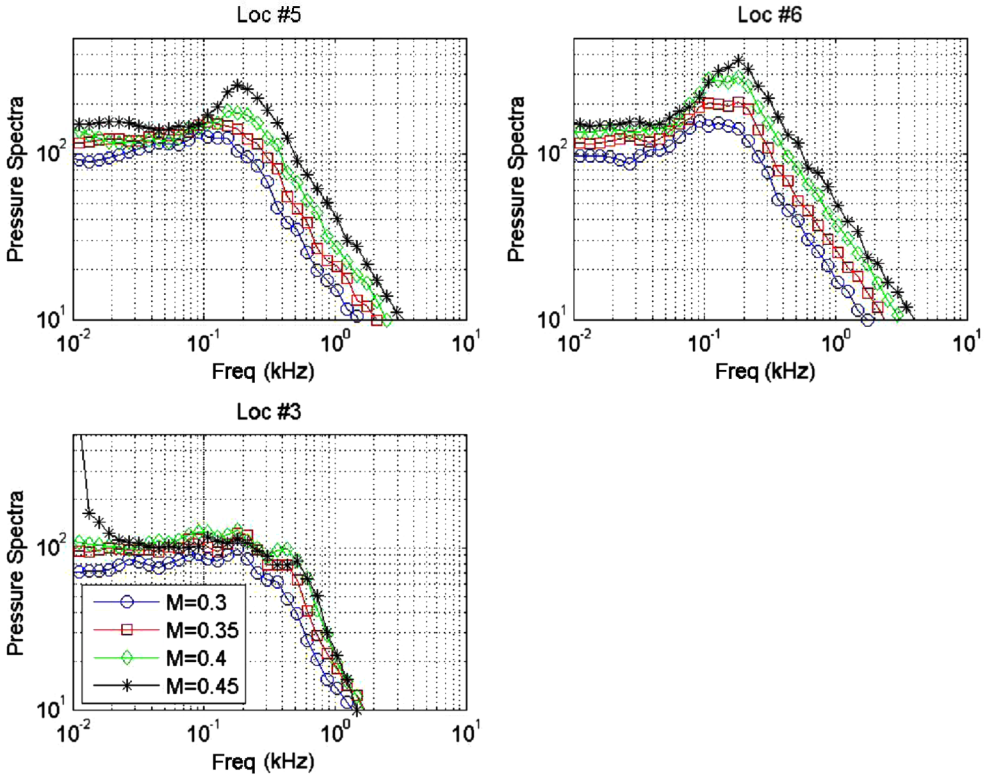

Fig. 7 Unsteady-pressure spectra for different sensors for several Mach numbers as a function of frequency.

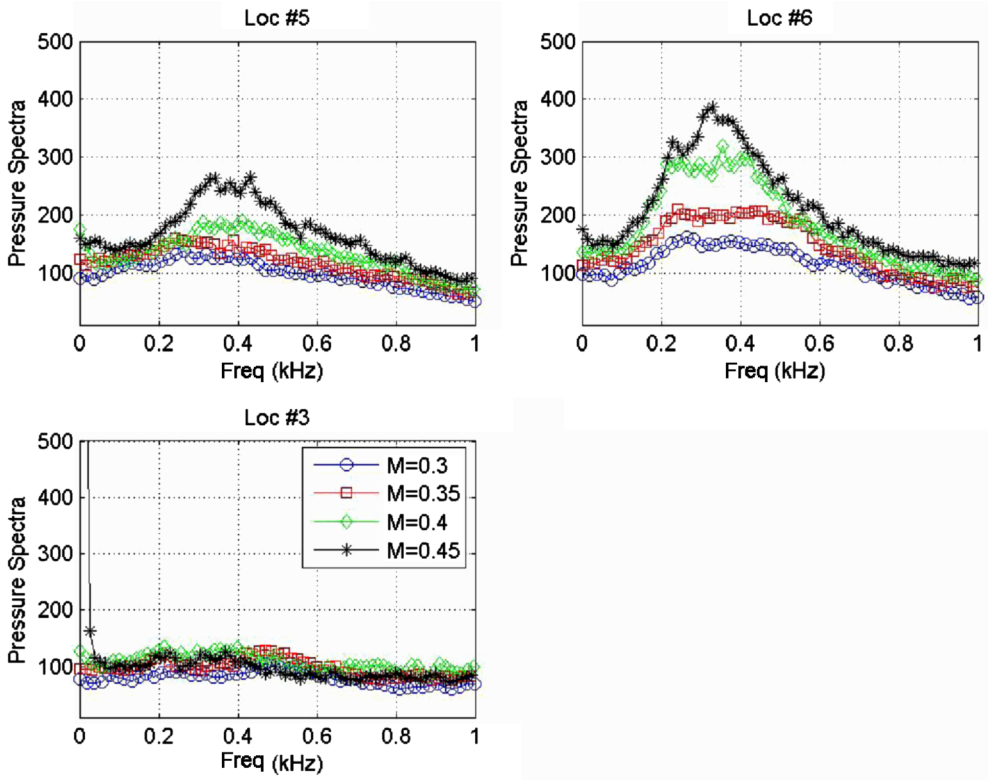

Fig. 8 Unsteady-pressure spectra for different sensors for several Mach numbers as a function of $St_D = fD/U_{\inf}$.

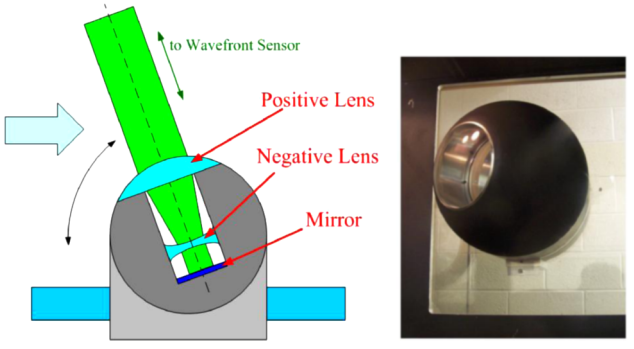

Fig. 9 Optical turret.

conduct extensive optical measurements. For the present study, test Mach numbers were chosen to be 0.35, 0.4, and 0.45.

Wind-tunnel tests were conducted on the conformal-window hemisphere-on-cylinder turret model shown mounted on the back wall of the tunnel in Fig. 2 (left). A cross-sectional dimensioned drawing is presented in Fig. 2 (right); all dimensions are in inches. The turret was placed on the back side of the test section, 54 in. downstream from the beginning of the test section. The 12-in.-diam turret was composed of a sphere mated to a cylindrical base 4.5-in. high. The hollow sphere was made of plastic and reinforced by adding epoxy material to create a thicker wall. The sphere was fitted with a flush-mounted positive lens with an outer radius of curvature that matched the 6-in. radius of the sphere. Details of the optical components will be discussed later. The sphere could be rotated along a vertical axis (i.e., zenith plane), thus allowing any elevation angle between 40 and 140 deg. The cylinder was mounted on a flat

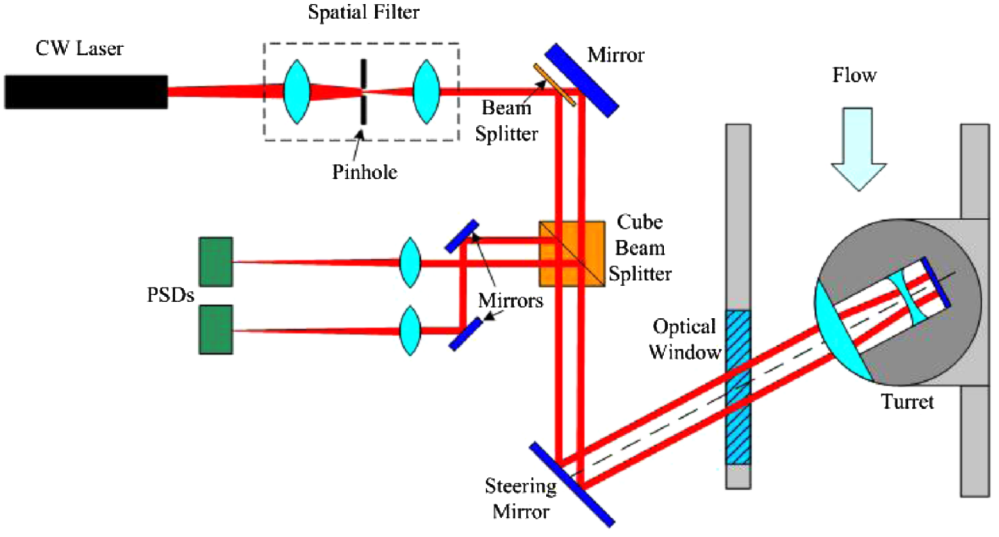

Fig. 10 Malley probe schematic.

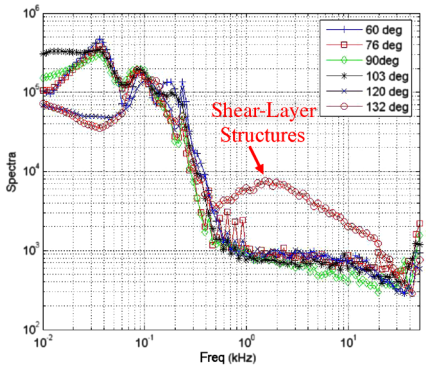

Fig. 11 Deflection-angle spectra for different elevation angles; $M = 0.4$.

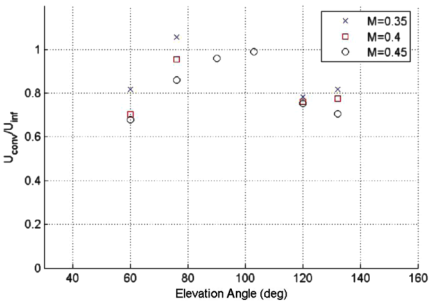

Fig. 13 Convective speeds of optical structures from the Malley probe.

plate and could be rotated to any azimuth angle. The open cylinder's end was sealed with a flat aluminum plate so that the interior of the turret was nominally at the test-section static pressure. The turret was also equipped with 10 static-pressure ports and three Kulite unsteady-pressure sensors: one mounted on the turret and two mounted on the mounting plate downstream of the turret.

A. Flow-Visualization Results

Surface-flow visualization was accomplished with a 1:2 mixture of rubbing alcohol (95% isopropyl alcohol) and Aeroshell Oil 100. This oil was chosen because it contains a fluorescent detergent visible under black light, readily highlighting flow patterns. The mixture was hand-sprayed from an aerosol bottle onto the turret and wall region in its vicinity, approximately 30 cm upstream and 100 cm downstream of the turret. This allowed visualization of body-surface flow and upstream turning and wake behavior. Once the mixture was applied, the tunnel was brought up to speed and held constant for 5–10 min. This allowed the mixture to mark the flow and a substantial amount of the alcohol to evaporate, stabilizing the patterns. As quickly as possible, the tunnel was shut down and opened, the black light shone on the wall, and photos taken before gravitational effects appreciably altered the flow patterns. Cleaners were then applied to the wall to remove the oil before a new run was initiated. Figure 3 shows the patterns under normal and black light.

Results of the oil-surface-flow visualization for different Mach numbers are presented in Fig. 4. Both the necklace vortex and the wake behind the turret have a complex topological structure. For example, the necklace vortex has two negative attractor lines nested between three positive attractors, which suggests a nested vortical structure inside of the necklace vortex. The wake behind the cylinder reveals the presence of the circulation bubble behind the turret, because streaklines travel upstream in this region. Flow on the downstream half of the turret also reveals a complex vortical structure, which weakly depends on the Mach number, as can be observed by comparing flow topologies on the turret for different Mach numbers in Fig. 4. This complex wake structure behind the turret imposes large levels of optical aberrations on the laser beam emanating from the turret in its aft quadrant.

B. Steady-Pressure Measurements

The hemispherical portion of the turret was equipped with a series of static-pressure ports 1 in. apart. Results of normalized static-pressure measurements along the turret center plane (at a 0-deg

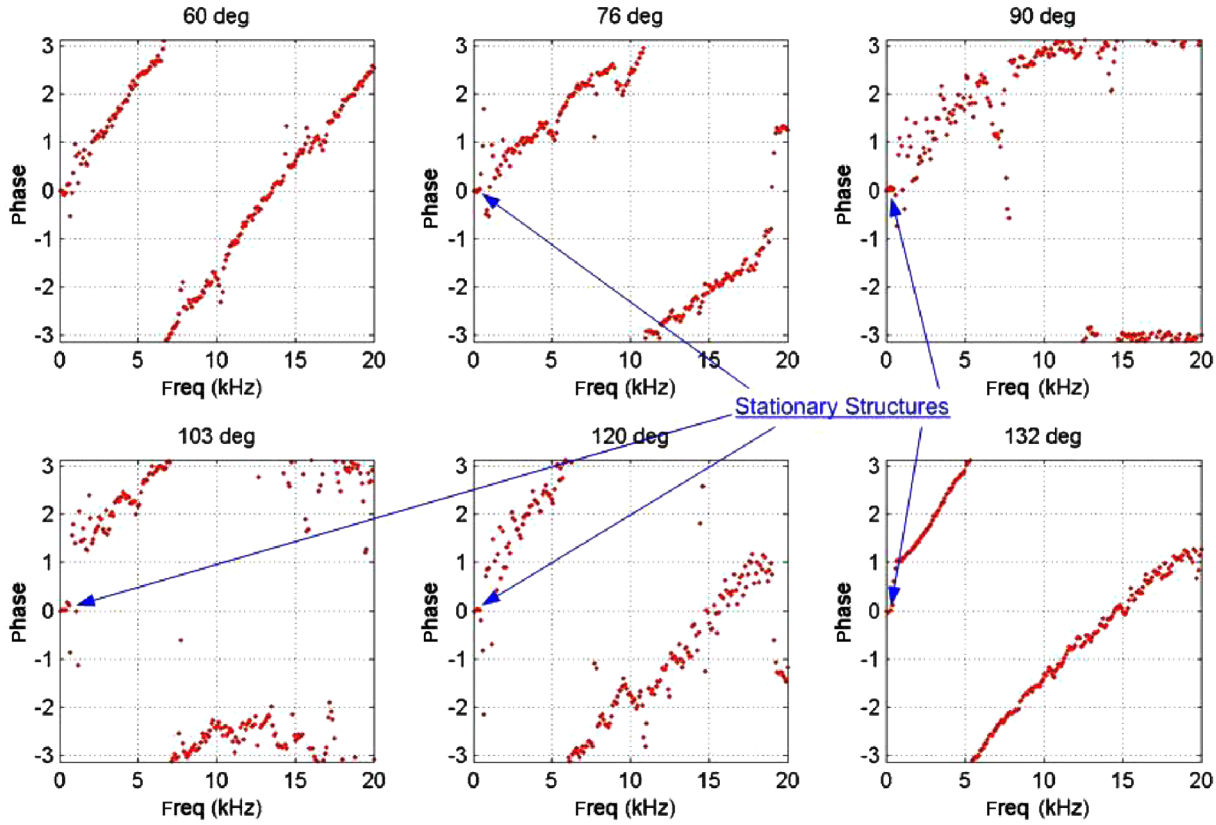

Fig. 12 Phase plots arg$[S(f)]$ for different elevation angles; $M = 0.4$.

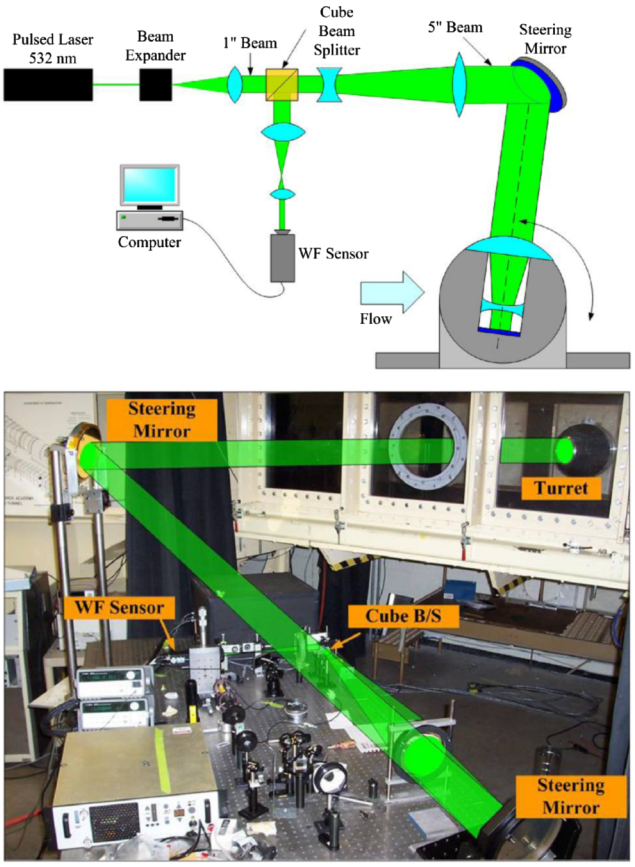

Fig. 14 Two-dimensional wave-front measurements: schematic (top) and optical setup (bottom).

azimuth angle) for different elevation angles and Mach numbers are presented in Fig. 5. An elevation angle of 0 deg corresponds to the upstream direction. Flow is stagnated at the junction of the hemispherical part of the turret (elevation angle of 0 deg), accelerates along the front portion of the turret and its cylindrical base (elevation angles between 0 and 90 deg), enters the region of an adverse pressure gradient on the back of the turret (elevation angles above 90 deg), and eventually separates after 115 deg.

C. Unsteady-Pressure Measurements

To characterize the temporal behavior of the wake behind the turret, three unsteady-pressure sensors were placed in the wake. Sensor 3 was placed on the mounting cylinder at an azimuth angle of $+135$ deg, 1.5 in. above the mounting plate. Sensors 5 and 6 were placed downstream of the turret at the tunnel wall at the locations shown in Fig. 6.

Unsteady-pressure power spectra for all three unsteady sensors at different Mach numbers are presented in Fig. 7. Pressures in the wake behind the turret, locations 5 and 6, exhibit a broad peak between 0.1 and 0.2 kHz, which increases in magnitude and shifts to higher frequencies with increasing Mach numbers. The turret-mounted sensor 3 shows the presence of several small broad peaks on the surface of turret. The same data replotted for nondimensional frequencies $St_D = fD/U_{\text{inf}}$ are shown in Fig. 8. The nondimensional wake spectra show a single peak at $St_D = 0.35$, independent of Mach number, corresponding to the vortex shedding behind the turret (i.e., the wake vortices indicated in Fig. 1). Small differences in pressure amplitudes might be due to a small flow asymmetry, because the turret was not mounted in the center of the back wall (see Fig. 2, right-hand side).

III. Optical Measurements

The turret was equipped with a set of lenses and a mirror, which were designed to return a coaxial collimated beam back to the optical

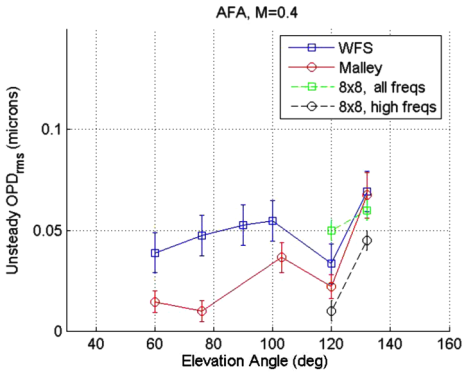

Fig. 15 OPD_{rms} with experimental uncertainties for different elevation angles for all measurement devices.

bench with minimal distortions (see Fig. 9). The optical system consists of three elements: a positive lens, a negative lens, and a flat mirror. The positive lens is 6 in. in diameter with a 5-in. clear aperture and has an outer radius of curvature of 6 in., mounted flush with the 6-in.-radius turret surface. The negative lens is mounted on an adjustable platform and is designed to compensate for a spherical aberration from the positive lens. The collimated beam passing through the flow, positive and negative lenses, is reflected by the flat mirror back through the same region of the flow, thus increasing the aberrations imposed on the beam by the flow by a factor of 2. The overall residual wave-front error of the optical system was less than $\lambda/8$ (at 633 nm) from peak to valley. Therefore, the optical system is equivalent to a flat mirror with a surface quality of $\lambda/8$.

Three different optical wave-front devices, a Malley probe, a commercial 2-D wave front sensor (WFS), and an 8×8 high-bandwidth wave-front sensor, were used to measure optical aberrations on a beam projected into and out of the turret at different elevation angles and Mach numbers in the zenith plane (i.e., a 0-deg azimuthal angle).

A. Malley Probe Results

The Malley probe principle of operation and data-reduction procedure can be found in [3,7,8]. Here, we briefly outline only the essential details. A schematic of the Malley probe optical setup is shown in Fig. 10. A small 1-mm-diam laser beam is split into two parallel laser beams spaced by 4 to 5 mm. The two beams are directed into and out of the optical turret via an optically flat beam-steering mirror. The optical turret reflects the beams coaxially (see the previous section), each along the same optical path back to the optical table. The returning beams are separated from the incoming beams at the optical bench using a cube beam splitter, and each beam is passed through a focusing lens onto position-sensing devices (PSDs). The PSDs measure each beam's instantaneous deflection angle by dividing the spot displacement by the focal length of the lens. The displacements are digitally acquired at a 200-kHz sampling rate for 10 s for postprocessing analysis, as outlined later.

The displacements are turned into angles and divided by two to account for the double pass and then stored as deflection angles $\theta_1(t)$ and $\theta_2(t)$. From these angles, the Fourier transform for each deflection angle $\theta_1(t)$ and $\theta_2(t)$ is computed and the cross-correlation function $S(f)$ is calculated: $S(f) = \langle \hat{\theta}_1^*(f)\hat{\theta}_2(f) \rangle$. Using the cross-correlation results, the zero-phase correlation in data is located and filtered out of deflection-angle data using a low-pass filter, as described in [5]. Then convective speeds U_c are determined by calculating a time delay between two signals and dividing this into the beam separation along the flow direction. Once the velocity is found, it is used to compute a time series of 1-D wave-front slices optical path difference [OPD(t)], assuming a frozen-field hypothesis: $\text{OPD}(t) = -U_c \int \theta_1(t)\, dt$. Time and position are then traded, again using the convective velocity, $x = -U_c t$, and the record is broken into aperture lengths A_p to obtain a time series of OPD(x) over the aperture. Each wave front then has its instantaneous

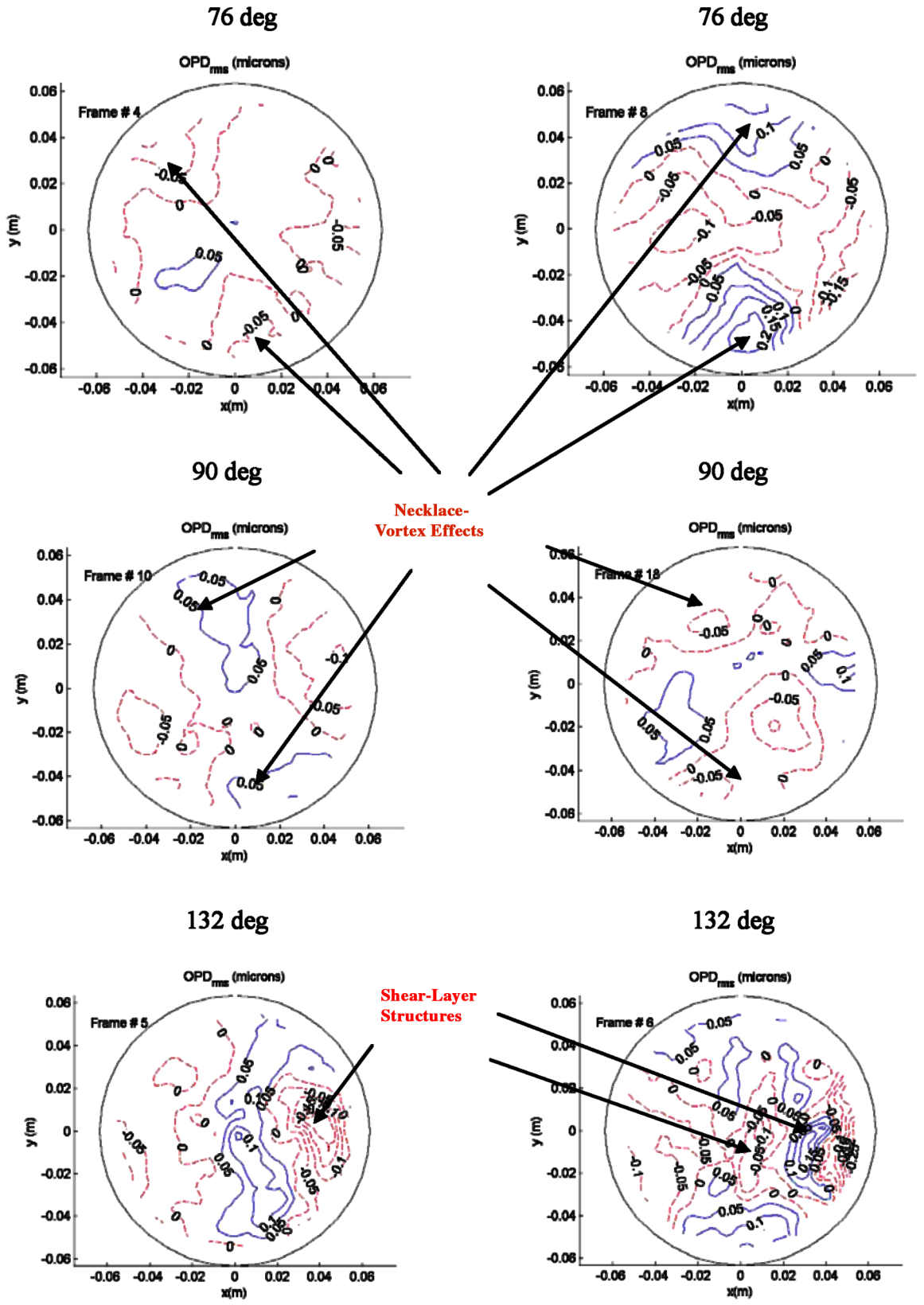

Fig. 16 Selected wave fronts for 76, 90, and 132 deg; $M = 0.4$; flow goes from left to right.

tilt component removed. Finally, residual OPD_{rms} over the aperture for each frame is computed and averaged over all frames.

Deflection-angle power-spectra plots for different elevation angles at $M = 0.4$ are presented in Fig. 11. Narrow peaks in spectra are due to electronic noise and may be ignored. Spectra for all angles have strong low frequency ($f < 0.7$ kHz) components. For elevation angles between 60 and 120 deg, spectra have quite similar shapes with dominant low frequencies. For the back-facing angle of 132 deg, the laser beam passes through a shear layer formed in the separation region behind the turret, and so the deflection-angle spectra have an additional, shear-layer-related peak around 2 kHz. Assuming the convective nature of the shear-layer structures and

using the convective speed as $U_c = 0.8$ and $U_{\text{inf}} = 130$ m/s (see the discussion about convective speeds later in this section), the typical structure size was found to be 130 m/s/2 kHz = 6.5 cm.

Phase delay between two deflection-angle time series (phase plots) for different elevation angles at $M = 0.4$ are presented in Fig. 12. All phase plots have a zero-phase correlation plateau at low frequencies below 0.8 kHz, as indicated in Fig. 12, suggesting the presence of stationary disturbances, that is, although it is unsteady, it is not convecting. The nature of these disturbances will be discussed later. All frequencies that had the character of a stationary disturbance were removed using a low-pass filter with a cutoff frequency of 0.8 kHz before reconstructing 1-D slices of wave fronts. Above 0.8 kHz, the phase plots show a linear dependence with frequency. This indicates a convective nature for the optically aberrating structures [3,7]. The presence of convective structures is evident for all elevation angles, even the forward-facing angles, suggesting a complex flow structure around the turret, although the inspection of phase data for all Mach numbers has revealed that the phase slopes are not well-defined for elevation angles of 90 and 103 deg, suggesting weak convective disturbances.

Knowing the phase slope, the average time delay τ between the two Malley probe beams can be found as $\arg[S(f)] = 2\pi f\tau$, and with the known beam separation in the streamwise direction, convective speeds of optically aberrating structures were calculated; these convective speeds are presented in Fig. 13. As already mentioned, at the elevation angles of 90 and 103 deg for $M = 0.35$ and 0.4, the convective speeds show large scatter (see Fig. 12), and so they are not presented in Fig. 13. Not surprisingly, flow accelerates over the front portion of the turret and decelerates on the back until it separates at around 115 deg. After this point, shear-layer structures appear in the separation region, with convective speeds of 0.8 of the freestream speed. These speeds are similar to the shear-layer convective speeds for the flat-window turret observed in [3].

B. Wave-Front-Sensor Results

Uncorrelated 2-D wave fronts across the turret aperture were taken using a WaveFront Sciences CLAS-2D two-dimensional wave-front system. A schematic and an annotated photograph of the optical setup are presented in Fig. 14. A frequency-doubled Nd:YAG laser with a pulse duration of 6 ns was expanded to a 5-in. collimated beam and directed from the optical bench to the test section using two large beam-steering mirrors. This beam was directed into the turret aperture radially and returned coaxially back to the bench. The return beam was then split using a cube beam splitter after being contracted to a 1-in. beam. The beam's optical distortions were measured using the 2-D Shack–Hartmann wave-front sensor with a 24 × 36 lenselet array. The wave fronts were sampled at 10 Hz. Two hundred wave fronts were recorded for each elevation angle and Mach number. Because of spherical aberrations imposed by the expanding optics, only a central 4.5-in.-diam portion was used to calculate wave-front error. Instantaneous tip/tilt was removed from each wave front, and an average aberration of the wave front over the aperture was calculated as OPD_{rms}.

OPD_{rms} from the 2-D wave-front sensor for different elevation angles at $M = 0.4$ are presented in Fig. 15. Also shown for comparison are results for OPD_{rms} from the Malley probe apertured to a 4.5-in. beam; the results from the high-bandwidth sensor, labeled 8 × 8, will be discussed later. The Malley probe and WFS results give similar values within experimental error for elevation angles above 120 deg. In this region, the dominant aberrations are the moving shear-layer structures.

Although a Malley probe can distinguish between stationary and traveling distortions, the Malley probe wave-front reconstruction, outlined earlier, relies on the frozen-flow hypothesis, and therefore, optical aberrations related to any stationary structure cannot be properly resolved using a Malley probe; it requires instantaneous wave-front measurements over the entire aperture, and a 2-D wave-front sensor is needed to investigate stationary aberrations. As such, any stationary (zero-phase correlation) portion of the optical signal, due to either vibration-related or aero-optical related effects, is removed from the Malley probe data using a low-pass filter, and only the convective part of the optical aberration can be reconstructed. It should be noted that the WFS results have tip/tilt removed so that the residual after tip/tilt removal has no vibration effects remaining. Because the Malley probe results are consistently lower than WFS results for all elevation angles below 100 deg, this suggests that unsteady, but stationary, aero-optical effects are present in this portion of the flow.

To investigate the nature of these stationary aberrations at forward-facing angles, selected wave fronts for elevation angles of 76, 90, and 132 deg at $M = 0.4$ are presented in Fig. 16. Small to moderate deviations (less than or equal to 0.12 μm) from a planar wave front can be observed on both sides of the aperture for the 76 and 90-deg cases. They are located approximately on both sides of the aperture and are in phase with each other. Because tunnel vibrations only add tip/tilt to wave fronts, which were subsequently

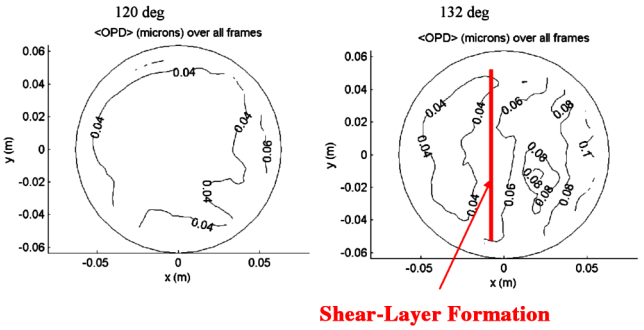

Fig. 17 Wave-front variations over the aperture for back-facing elevation angles; $M = 0.4$; flow goes from left to right.

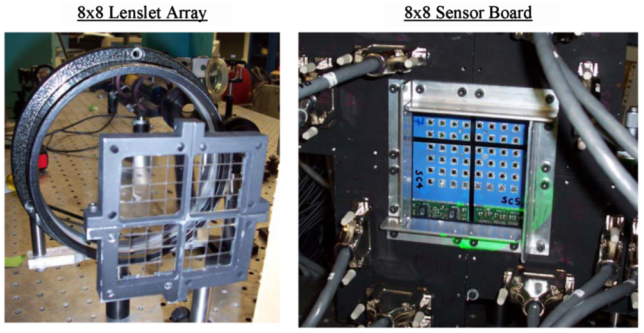

Fig. 18 High-bandwidth wave-front sensor.

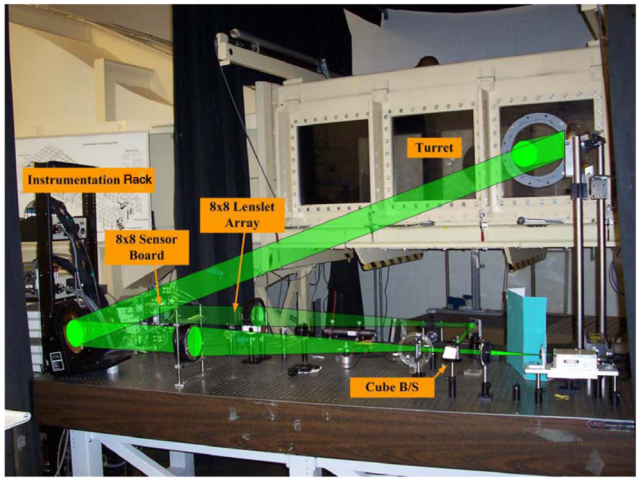

Fig. 19 High-bandwidth wave-front sensor optical setup.

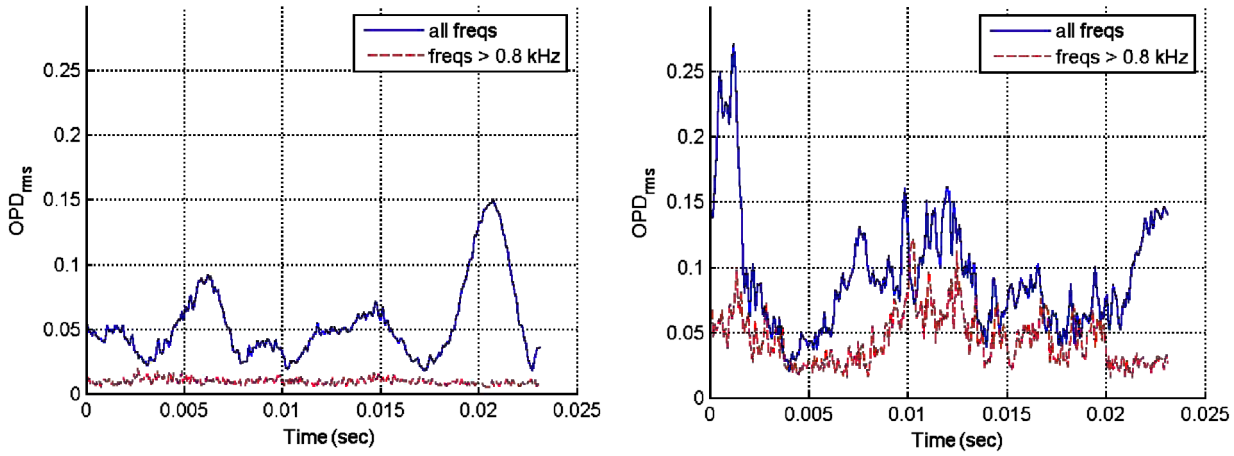

Fig. 20 Temporal evolution of OPD_{rms} from the 8 × 8 sensor for the 120-deg (left) and 132-deg (right) cases; $M = 0.4$.

removed from WFS data, we hypothesize that these aberrations may be due to the interaction of the turbulent wake behind the turret, with the necklace vortex formed at the bottom front portion of the turret. These necklace-vortex-related, low-frequency motions modify the potential flow around the turret and create unsteady, but *stationary*, distortions on the laser beam. These stationary aberrations are removed from the Malley probe data, which results in underpredicting overall optical aberrations using the Malley probe at forward-facing angles (see Fig. 15). It is worth noting that these stationary distortions are clearly geometry-related; additional studies are needed of how different turret geometries and flow-modifying devices (such as a collar or a splitter plate around the cylindrical base, for instance) affect optical environments around turrets.

After the flow separates at 115 deg, spanwise shear-layer structures appear downstream of the separation location. These are clearly visible for the 132-deg case in Fig. 16. To better see the spatial growth of the shear-layer structure, temporally averaged wave fronts, $\langle \mathrm{OPD} \rangle$, over the aperture for the 120 and 132-deg cases for $M = 0.4$ were computed and are presented in Fig. 17. For the 120-deg case, $\langle \mathrm{OPD} \rangle$ is uniform over the aperture, with levels of 0.04 μm. At 132 deg, $\langle \mathrm{OPD} \rangle$ is around 0.04 μm for the front half of the aperture and increases downstream, starting from the middle of the aperture. This marks the onset of the shear-layer structure formation. A linear growth of the shear layer leads to an observed linear increase in wave-front amplitudes at the downstream half of the aperture.

C. High-Bandwidth Wave-Front-Sensor Results

A high-bandwidth wave-front sensor was also used to measure the temporal–spatial evolution of wave fronts. The 8 × 8 subaperture, high-bandwidth wave-front sensor is a further development of the 4 × 4 subaperture high-bandwidth wave-front sensor jointly developed with Oceanit [9]. It is a Hartmann-type wave-front sensor with an 80 × 80 mm, 8 × 8 lenslet array (Fig. 18, left) and an 8 × 8 square array of analog position-sensing devices to measure beam centroids (Fig. 18, right). The analog nature of the data acquisition board allows wave-front sampling rates in excess of 100 kHz; however, a sampling rate of 78 kHz was used in this series. Because of experimental time constrains, only two elevation angles of 120 and 132 deg were investigated.

The high-bandwidth wave-front sensor optical setup is shown in Fig. 19. A continuous wave frequency-doubled Nd:YAG laser beam was expanded to 5 in., similar to the WFS optical setup in Fig. 14, and transmitted through the flow to the turret. The reflected beam was returned coaxially to the bench, and after contraction back to a 1-in. beam, it was split using a cube beam splitter and then reexpanded onto the 8 × 8 wave-front sensor. Because of spherical aberrations near the beam edges, only the middle portion of the returned beam with a diameter of 3_in. (i.e., less than the 4.5-in. aperture used for a 2-D wave-front sensor) was used to reconstruct the wave fronts as follows:

Displacement voltages from the sensors at the lenselet focal plane (two channels per sensor, for a total of 128 channels) were sampled at 78 kHz for 10 s. Using calibration constants, the signals were converted to deflection angles and divided by two to give $\theta_i(t)$, for each location. The deflection angles' time histories were filtered using either a low- or high-pass filter to separate stationary and convecting structures. The wave fronts were then computed from deflection angles, $\mathrm{WF}(t) = \mathrm{grad}[\theta_i(t)]$. The piston and tip/tilt modes were then removed from each wave front. The steady or mean wave front was computed over all wave fronts and was removed from each wave front. The resulting wave fronts then reflected only the *unsteady* components.

By filtering the wave-front gradients using the low-pass filter, wave fronts could be reconstructed that contained only the stationary aberrations, and by filtering the gradients with a high-pass filter, wave fronts could be reconstructed that contained only the convecting distortions. The temporal evolution of the OPD_{rms} over the aperture at $M = 0.4$ are presented in Fig. 20. Both high-pass (above 0.8 kHz) filtered and unfiltered cases for two angles, 120 and 132 deg, are shown. For the 120-deg case, most of the optical aberrations are located at low frequencies (below 0.8 kHz). These exhibit large-amplitude, low-frequency (of the order of the turbulent wake) deviations. This is due to the low-frequency unsteady pressure and thus density variations in the potential field around the turret, which we hypothesized were due to the large-scale wake unsteadiness communicated forward through the necklace-vortex–wake interaction around the turret base. High frequencies (above 0.8 kHz) are responsible only for a small portion of the optical aberrations for this angle; however, for the 132-deg case, the high shear-layer-related frequencies cause most of optical aberrations. The lower-frequency wake-related disturbances only occasionally influence the optical distortions at this angle.

As discussed earlier, based on the Malley probe data, we expect that the unsteady, but stationary, necklace-vortex effects and their association with entrainment into the unsteady wake are the main cause of optical aberrations for frequencies below 0.8 kHz; moving shear-layer structures dominate optical distortions for all frequencies above 0.8 kHz. Further understanding of these low- and high-pass-filtered wave fronts can be gained by examining selected wave fronts, as in Fig. 21. Two time instances are shown in Fig. 21, marked by dashed lines on the middle plot, indicating all- and high-frequency components of the wave front, and the arrows indicate where these occur in the wave front's time series (flow again goes from left to right). For the low-frequency part of the wave front, necklace-vortex effects are clearly present on both sides of the aperture. The high-frequency component of the wave front reveals shear-layer structures convecting across the aperture.

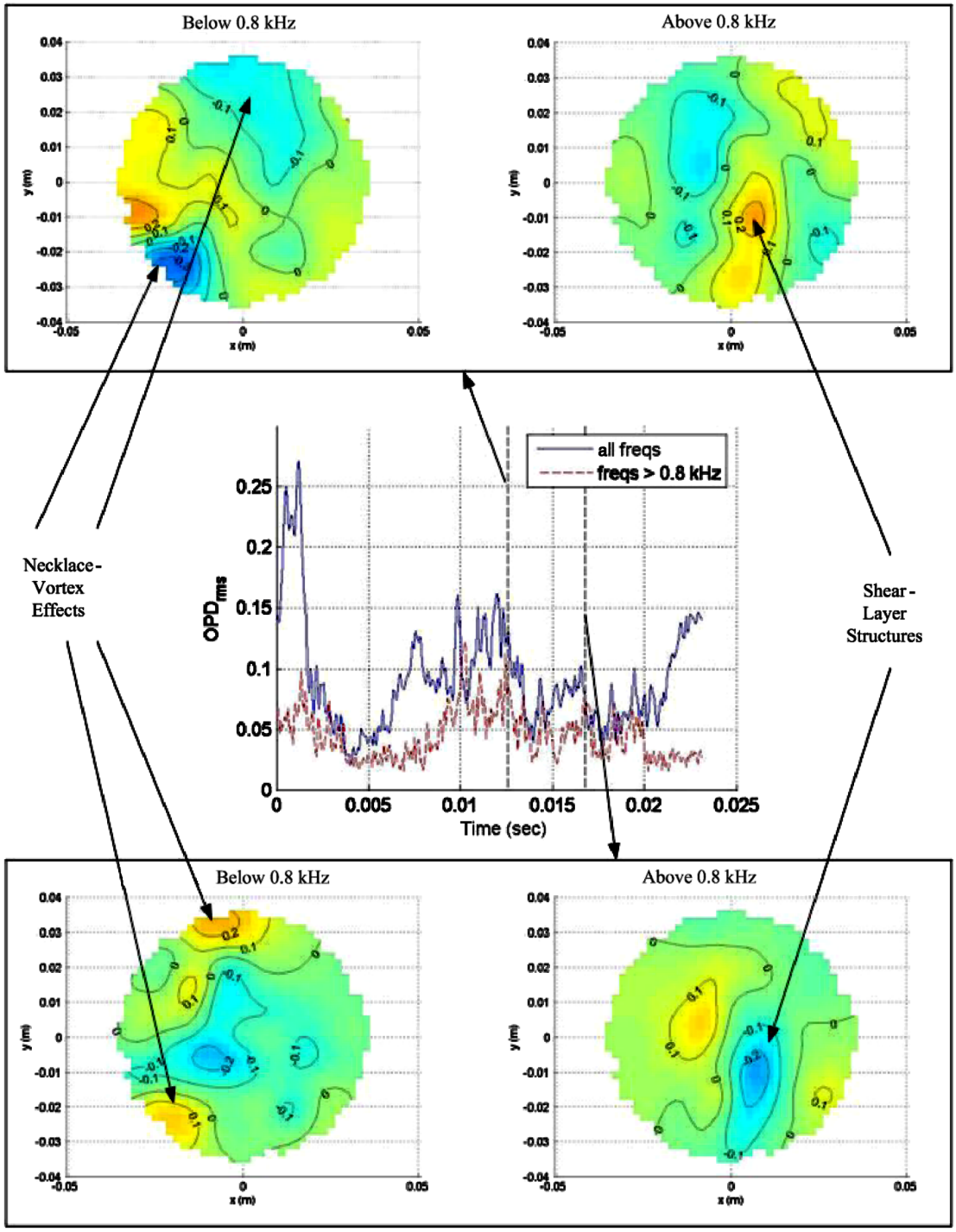

Fig. 21 Reconstructed wave fronts for low (below 0.8 kHz) and high (above 0.8 kHz) frequencies from the 8 × 8 high-bandwidth wave-front sensor; elevation angle is 132 deg; $M = 0.4$.

A summary of the time-averaged optical measurements using all three sensors is presented in Fig. 15. Referring to this figure, the unfiltered 8×8 sensor data over a 3-in. aperture (labeled "all freqs") at elevation angles of 120 and 132 deg are similar, within experimental error to the WFS results over a 4.5-in. aperture, and give about 0.07 μm of optical aberrations at the elevation angle of 132 deg at $M = 0.4$. The high-pass-filtered 8×8 sensor results, labeled "high freqs," are similar to the Malley probe data over a 4.5-in. aperture, because neither includes stationary effects. Small differences between the high-frequency 8×8 sensor and the Malley probe results can be contributed to different aperture sizes for the Malley probe and 8×8 sensor, as well as uncertainties in the calculation of convective speed, which directly affect the accuracy of the Malley probe results (see Sec. III.A). Overall, optical aberrations are high for backward-facing angles, in which the structures in the separated shear layer play a dominant role.

Compared with the high spatially resolved wave-front measurements at 132 deg using the WaveFront Sciences wave-front sensor, Fig. 15 suggests that 8×8 subapertures are sufficient to resolve the main components of shear-layer structures, but fine details are obviously missing. Therefore, the high temporal resolution and analog nature of the output signal allows isolating and inspecting wave-front components at different frequency bands and separating stationary disturbances, such as unsteady-wake and necklace-vortex far-field effects, from convective aberrations, such as the shear-layer structures. A high-spatial-resolution 2-D wave-front sensor having

hundreds of subapertures cannot currently separate stationary and moving components of the optical wave front directly. Thus, the 8×8 high-bandwidth sensor combines the high temporal resolution and analog nature of the output signal, typical for the Malley probe, and a decent spatial resolution, such as a conventional 2-D wave-front sensor. This ability of the 8×8 sensor to reconstruct corresponding wave fronts for different frequency bands has now proven to be able to provide valuable information about the flow that is invaluable to adaptive-optic analysis and design and is not available by other means.

IV. Conclusions

This paper complements an earlier paper [3] that examined a similar turret, but with a flat window. In the present study, the flat window was replaced with a conformal window. This seemingly minor change in the turret, from an optical point of view, greatly modified the environment from that of the flat-windowed turret in the aft quadrant. Whereas in the flat-windowed case, the flow separation was fixed by the surface-slope discontinuity, in the conformal case, the separation line becomes unsteady. On the positive side, the conformal window extends the useful field of regard to approximately 120 deg. On the negative side, the added complexity of the conformal-window flow makes for a more unpredictable optical environment.

This paper also underscores the importance of using a suite of optical instruments to access the optical environment around turrets. The use of the Malley probe allowed for highly spatially and temporally resolved 1-D slices of OPD data for the highest-frequency convecting aberrations in the flow. The high spatial detail of the convectional 2-D wave fronts provides information about the small-scale aberrations in the flow, but usually operates under low sampling rates and thus provides only uncorrelated snapshots of wave fronts. This conventional sensor could not provide a rationale for the differences between Malley probe data and 2-D wave fronts for elevation angles less than 120 deg. Through analysis techniques developed during this study, the high-bandwidth, 8×8, 2-D, wave-front sensor was able to explain these differences and add greatly to our understanding of the complex flow physics creating the optical environment. Finally, the pressure and flow-visualization data added confidence to the understanding we have given here.

Acknowledgments

These efforts were partially sponsored by the High Energy Laser Joint Technology Office (JTO) and the U.S. Air Force Academy. The U.S. Government is authorized to reproduce and distribute reprints for governmental purposes, notwithstanding any copyright notation thereon.

References

[1] Gilbert, K. G., "Overview of Aero-Optics," *Aero-Optical Phenomena*, edited by K. G. Gilbert and, L. J. Otten, Vol. 80, Progress in Astronautics and Aeronautics, AIAA, New York, 1982, pp. 1–9.

[2] Jumper, E. J., and Fitzgerald, E. J., "Recent Advances in Aero-Optics," *Progress in Aerospace Sciences*, Vol. 37, No. 3, 2001, pp. 299–339.

[3] Gordeyev, S., Hayden, T., and Jumper, E., "Aero-Optical and Flow Measurements over a Flat-Windowed Turret," *AIAA Journal*, Vol. 45, No. 2, 2007, pp. 347–357.

[4] Tyson, R. K., *Principles of Adaptive Optics*, Academic Press, San Diego, CA, 1991.

[5] Van Dyke, M., *An Album of Fluid Mechanics*, Parabolic Press, Stanford, CT, 1982, pp. 34–35.

[6] Cress, J., Gordeyev, S., Jumper, E., Ng, T., and Cain, A., "Similarities and Differences in Aero-Optical Structure over Cylindrical and Hemispherical Turrets with a Flat Window," 45th Aerospace Science Meeting and Exhibit, Reno, NV, AIAA Paper 2007-0326, 2007.

[7] Malley, M., Sutton, G. W., and Kincheloe, N., "Beam-Jitter Measurements for Turbulent Aero-Optical Path Differences," *Applied Optics*, Vol. 31, No. 22, 1992, pp. 4440–4443.

[8] Duffin, D., Gordeyev, S., and Jumper, E., "Comparison of Wave Front Measurement Techniques on a Two-Dimensional Heated Jet," 35th AIAA Plasmadynamics and Laser Conference, Portland, OR, AIAA Paper 2004-2446, 2004.

[9] Gordeyev, S., Duffin, D., and Jumper, E., "Aero-Optical Measurements Using Malley Probe and High-Bandwidth 2-D Wave Front Sensor," *International Conference on Advanced Optical Diagnostics in Fluids, Solids and Combustion (VSJ–SPIE '04)* [CD-ROM], Vacuum Society of Japan, Tokyo, Japan, 2004, Paper V0020.

R. Lucht
Associate Editor